THE ASTROPHYSICAL JOURNAL, 368:12–27, 1991 February 10

SIMULATED OPTICAL IMAGES OF GALAXIES AT $z \sim 1$ USING ULTRAVIOLET IMAGES OF NEARBY GALAXIES

RALPH C. BOHLIN
Space Telescope Science Institute, Homewood Campus, Baltimore, MD 21218

ROBERT H. CORNETT, JESSE K. HILL, ROBERT S. HILL, AND WAYNE B. LANDSMAN
ST Systems Corporation, 4400 Forbes Boulevard, Lanham, MD 20706

ROBERT W. O'CONNELL
Astronomy Department, University of Virginia, P.O. Box 3818, Charlottesville, VA 22903-0818

AND

SUSAN G. NEFF, ANDREW M. SMITH, AND THEODORE P. STECHER
Laboratory for Astronomy and Solar Physics, NASA/Goddard Space Flight Center, Code 680, Greenbelt, MD 20771
Received 1990 April 10; accepted 1990 August 1

ABSTRACT

Ultraviolet sounding rocket images of several nearby galaxies are used to simulate the appearance in optical bandpasses of similar systems at redshifts $z = 0.5$–2.67, as observed by the WFPC on HST and by ground-based instruments. Since the morphology of galaxies is a strong function of the wavelength, the appearance of galaxies at large redshifts is subject to a large k-correction effect. The strong dependence of monochromatic surface brightness on redshift $[I_\lambda \sim (1+z)^{-5}]$ also implies that observed morphology of distant systems will be crucially dependent on the limiting surface brightness set by the sky background. Although the angle subtended by sources depends only weakly on z, the fraction of a galaxy whose surface brightness is above the detection threshold varies strongly with z. Morphological distinctions of spiral from elliptical, spiral from irregular, and barred from unbarred types become more difficult, as does accurate evaluation of interactions or of the local environment.

Subject headings: cosmology — galaxies: photometry — galaxies: structure — ultraviolet: spectra

1. INTRODUCTION

Morphology plays a central role in the assessment of the evolutionary state of galaxies and will be particularly important in clarifying the early stages of evolution, which can be observed at high redshifts. Subarcsecond imaging of very distant objects at large lookback times has recently become feasible at good ground-based sites (Thompson 1988; Le Fèvre & Hammer 1988; Hutchings & Neff 1990, and references therein) and will also be a major emphasis of *Hubble Space Telescope* observing programs. Because the appearance of a galaxy is a very strong function of wavelength, morphological studies of distant galaxies will be seriously complicated by the k-correction, i.e., the difference in the object's spectral energy distribution between the rest wavelength and the observed wavelength. The k-correction is large, even in the absence of significant evolutionary changes in the stellar population. For instance, a galaxy similar to a local Sb, when viewed in the V band at a redshift $z \sim 1$, might have a doughnut-like appearance, because the k-correction for the cool stars in the bulge will be much larger than for the warm stars in the disk (e.g., Pritchet & Kline 1981; Bruzual 1988).

The prediction of optical-band morphologies at high redshift requires near-UV images of nearby galaxies in the 2500 Å range, which is redshifted into the B or V observing bands at $z \sim 0.75$ and $z \sim 1.20$, respectively. At present, there is little such information available. Earlier work on this problem (e.g., Pritchet & Kline 1981; Weedman & Williams 1987; Bruzual & Kron 1980; King & Ellis 1985) utilized *OAO 2*, *IUE*, or other UV spectrophotometric data, which in general have little spatial resolution or, in the case of *IUE*, only limited spatial extent owing to the small (10″ × 20″) entrance aperture.

The production of a suitable set of UV galaxy images covering a wide range of Hubble types is one of the primary goals of the Ultraviolet Imaging Telescope, to be flown on the Spacelab Astro missions (Stecher et al. 1983). In the meantime, we can employ the images obtained by sounding rocket prototypes for the UIT to simulate the appearance of high-redshift objects, even though the images are inferior in quality to those which will be obtained by UIT or HST.

Sounding-rocket UV images of five nearby spiral galaxies, with ∼15″ resolution, were obtained in the UIT prototype program, and details on most of these have been published (see Table 1). Included were M101, M83, M31, M51, and M33. All five galaxies were imaged in a broad (∼1000 Å) passband centered at ∼2500 Å. M31, M33, and M83 were also imaged in a band of intermediate width (∼350 Å) centered in the far-UV at ∼1500 Å. In addition, images of the Virgo cluster with ∼1′–2′ resolution have been obtained with a rocket-borne wide field Schwarzschild camera (Smith & Cornett 1982). The Virgo cluster field was imaged in a single wide bandpass centered at ∼2500 Å.

In all cases, the detectors employed ITT microchannel plate image intensifiers, coupled with fiber optics to Kodak II-aO film. The film images were digitized using a PDS microdensitometer. The images were linearized and flat-fielded using data obtained in the laboratory. A thorough discussion of the data reduction procedures is given by Bohlin et al. (1982) and Hill (1987).

Figures 1*a* and 1*b* illustrate the large differences in morphology between the UV and optical images of spiral galaxies. These differences mimic the large effects of differing redshifts on the observed morphology of otherwise identical spiral gal-

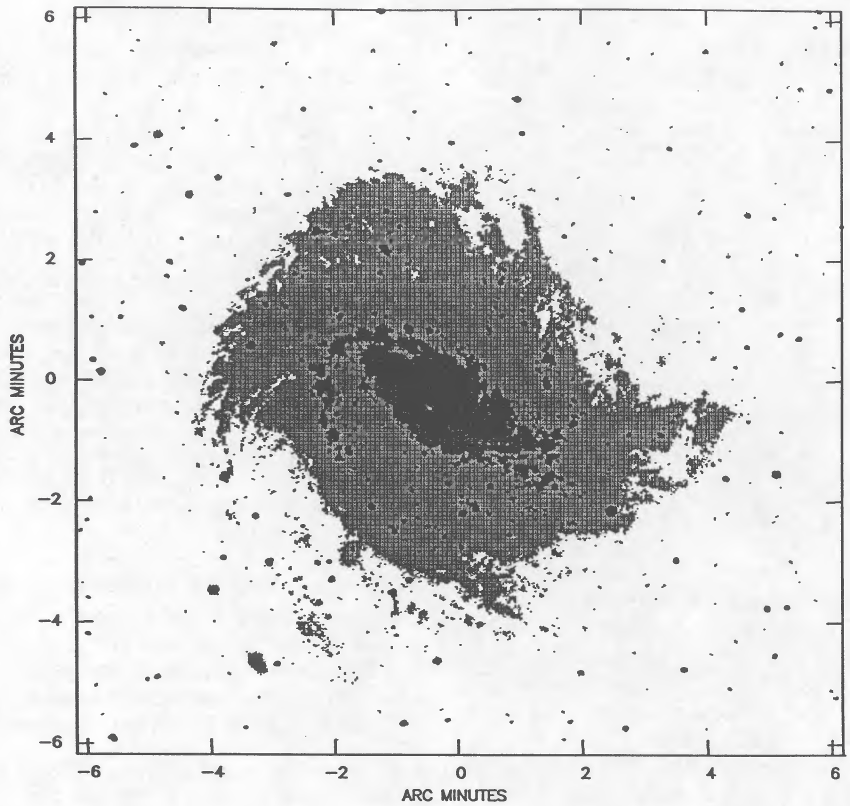

FIG. 1*a*

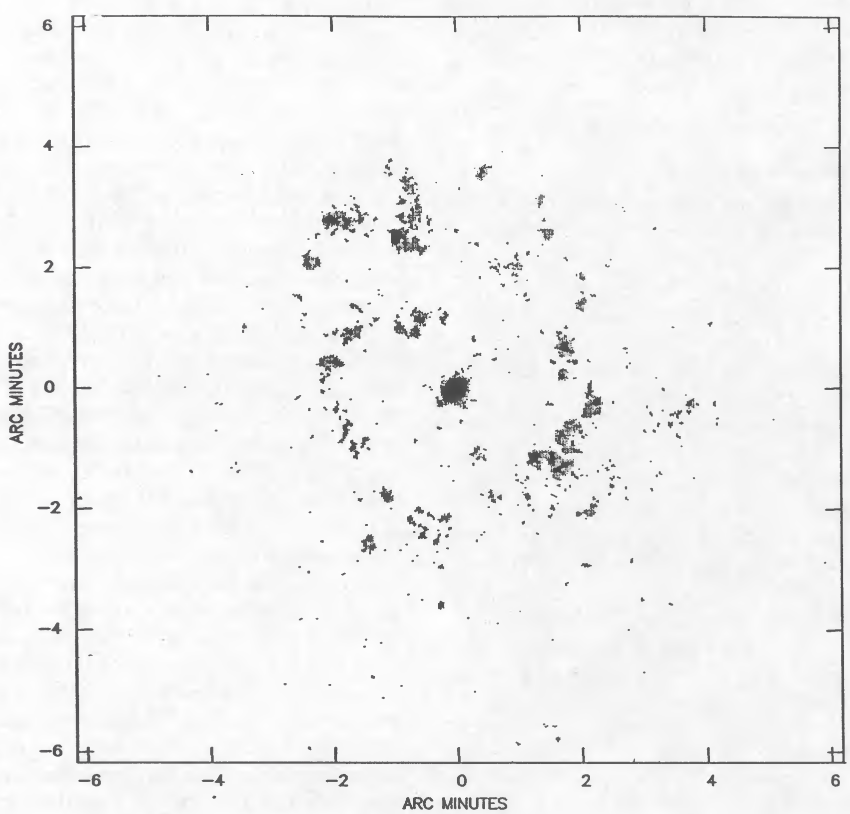

FIG. 1*b*

FIG. 1.—**Images of the spiral galaxy M83 in (*a*) the ground-based *V* band and (*b*) the far-UV band, illustrating the differing morphologies expected for otherwise identical spiral galaxies observed optically at redshift 0 and 2.67. North is at the top, and east is at the left in all figures in this paper.**

TABLE 1

SOUNDING ROCKET UV IMAGES OF GALAXIES

Galaxy	Hubble Type	Resolution	D (Mpc)	FNUV[a]	Reference
M101	Sc(s) I	15″	7.2	12.0	1
M51	Sbc(s) I–II	15	9.6	6.8	2
M31	Sb(s) I	15	0.7	55.5	3
M33	Sc(s) II–III	15	0.7	146	4
M83	SBc(s) II	15	3.75	15.3	5
M87	E0	100	20	0.16	6
M100	Sc(s) I	100	20	1.7	6
N4472	E1	100	20	0.16	6
N4254	Sc(s) I	100	20	1.6	6
N4647	Sc	100	20	0.23	6
N4649	E0	100	20	0.20	6
N4569	Sab	100	20	0.26	6
IC 3583	Sm III	100	20	0.20	6

[a] All tabulated fluxes in units of $\times 10^{-13}$ ergs s^{-1} cm^{-2} Å^{-1}.

REFERENCES.—(1) Stecher et al. 1982; (2) Bohlin et al. 1990a; (3) Bohlin et al. 1985; (4) Landsman et al. 1990; (5) Bohlin et al. 1983; (6) Smith & Cornett 1982.

axies observed in a fixed band. Figure 1*a* shows the *V* band image of M83 obtained by Talbot, Jensen, and Dufour (1979). The bar in the inner regions and the broad spiral arms are prominent features in this image. Figure 1*b* shows the far-UV sounding rocket image obtained by Bohlin et al. (1983). In this image, the bar consists mostly of cool stars and is invisible. The nuclear starburst and the OB associations in the outer spiral arm regions are prominent. If a galaxy identical to M83, but at a redshift $z = 2.67$, were observed in the *V* band with comparable effective spatial resolution, its appearance would be similar to the M83 far-UV image.

In § II, the methods used to construct the simulated images of systems at high redshift are discussed. Contour maps and fluxes are presented. Important implications of the simulations are discussed in § III.

2. SIMULATED IMAGES OF GALAXIES AT HIGH REDSHIFT

2.1. *Technique*

Our goal is to simulate the spatial resolution and surface brightness of high-redshift galaxies in selected optical observing bands. However, we make no attempt to correct for the evolution of the stellar populations, so the simulations represent the appearance of *current* epoch galaxies viewed at large distances.

The smallest resolvable features in the UV galaxy images obtained by the UIT prototypes (with $\sim 15''$ resolution) are smaller than the smallest resolvable features in an optically observed galaxy at $z \sim 1$, even for observations using the Wide Field/Planetary Camera (WFPC) on the Hubble Space Telescope (HST). Thus, the sounding rocket UV galaxy images can be used to simulate optical band observations of similar systems at high redshift obtained by any existing or planned observing facilities.

For example, the M51 UV images (Bohlin et al. 1990a) have a physical size per resolution element of 700 pc at the distance of M51 (9.6 Mpc). The angular size θ_z corresponding to the physical size L at redshift z can be computed from the relation

$$\theta_z = \frac{(H_0/c)L(1+z)^2 q_0^2}{q_0 z + (q_0 - 1)(\sqrt{1 + 2q_0 z} - 1)} \qquad (1)$$

(Peebles 1971), which gives $\theta_z = 0\overset{''}{.}13$ for $L = 700$ pc, $H_0 = 67$ km s^{-1} Mpc^{-1}, $q_0 = 0.5$, and redshift $z = 0.5$. Since θ_z is comparable with the angular resolution of the HST Wide Field Camera, the UV images simulate HST optical band observations at $z \sim 1$.

Because θ_z is much less than the angular resolution of the highest resolution ground-based observations now commonly obtainable ($\sim 0\overset{''}{.}7$), use of the UV images to simulate such optical observations at $z \sim 1$ requires degrading the resolution by a factor determined from the relation:

$$f = \mathrm{FWHM}_V/\theta_z , \qquad (2)$$

where FWHM_V is the angular resolution of the optical data being simulated and θ_z is the angle subtended by a source at redshift z whose physical size is the same as that corresponding to a resolution element of the input UV image.

In summary, imaging observations at a given redshift z can be simulated by performing three steps:

1. Specify the cosmological model by choosing values of the Hubble constant H_0 and the deceleration parameter q_0, assuming a Friedman model with zero cosmological constant.
2. Determine the ratio between the angular scale of the observed galaxy and the angular scale of an identical galaxy at the simulated redshift.
3. Determine the factor by which the resolution of the UV image must be degraded in order to simulate observations by the instrument to which the simulations apply.

The angle subtended by a source of fixed linear size attains a relative minimum at a redshift $z = 1.25$, for $q_0 = 0.5$ (Peebles 1971). The angle subtended by a source of fixed linear size varies weakly with z over the redshift range simulated here.

Computations presented here have been performed assuming $\mathrm{FWHM}_V = 0\overset{''}{.}70$ for the ground-based simulations based on the UIT precursor images. Such resolutions have been attained in imaging of distant galaxies by, e.g., Le Fèvre & Hammer (1990). For the simulated HST WFPC observations, we have assumed a resolution of $0\overset{''}{.}10$. We have specified the cosmological parameters by choosing $H_0 = 67$ km (s Mpc)$^{-1}$ (Rowan-Robinson 1985) and $q_0 = 0.50$, appropriate for the "inflationary" universe (Guth 1981). If $q_0 = 0.10$, the smoothing factors increase by 10% at $z = 0.5$, and 20% at $z = 1.0$.

Simulations at both HST and ground-based resolution have been derived from the 2500 Å band images of the galaxies observed by the UIT prototypes for three redshifts: $z = 0.5$, 0.75, and 1.2. The wavelengths of observation [equal to $2500(1 + z)$] are then 3750, 4375, and 5500 Å, roughly equivalent to the central wavelengths of the *U*, *B*, and *V* bands, or to the "photometric set" of WFPC filters (Griffiths 1985). The near-UV rocket bandpass is much broader relative to the wavelength of peak sensitivity ($\Delta\lambda/\lambda \sim 0.4$) than the optical bandpasses. However, *IUE* spectra of star-forming regions of M101 (Hill, Bohlin & Stecher 1984) and M83 Bohlin et al. 1983) indicate that there should not be strong bandwidth-dependent effects in the simulations.

Images of the Virgo Cluster at $z = 0.004$ (Smith & Cornett 1982) were obtained by a wide-field instrument (field size $11\overset{\circ}{.}4$) with much lower resolution (FWHM $\sim 100''$) than the UIT prototypes. If the resolution of the simulated optical images is assumed to be $1\overset{''}{.}9$ (FWHM), f is near unity. We conclude that the image presented by Smith & Cornett (1982) at its original resolution simulates the appearance of a galaxy cluster at redshift 0.5–1.2 in optical bands with typical ground-based resolution.

Approximately 200 galaxies are detectable in the wide-field

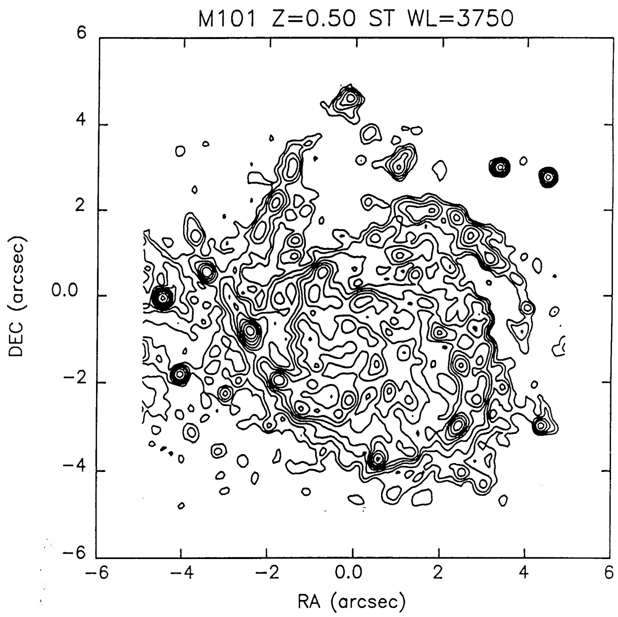

FIG. 2a

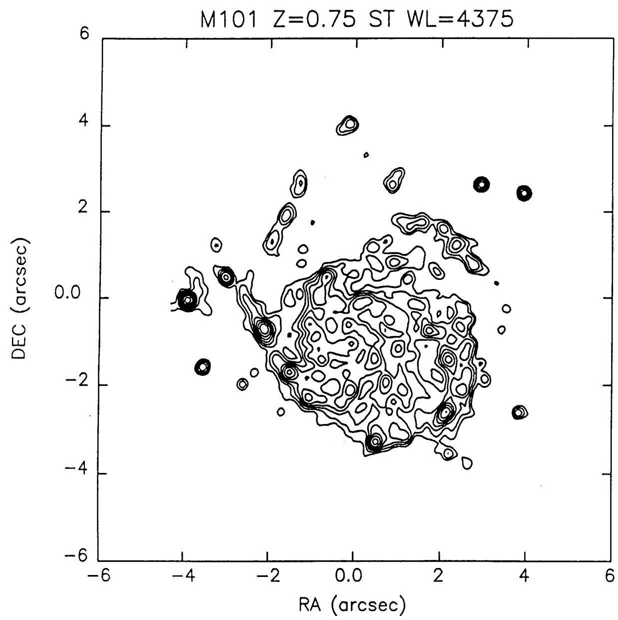

FIG. 2b

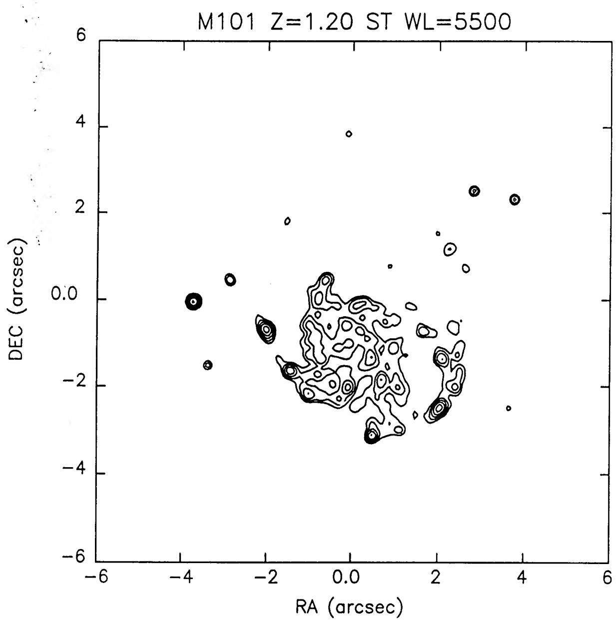

FIG. 2c

FIG. 2.—Contour maps at HST WFPC resolution of simulations based on UIT-prototype images of M101 for (a) $z = 0.5$, (b) $z = 0.75$, and (c) $z = 1.2$. In all maps, the lowest contour level surface brightness is 3.0×10^{-20} ergs s^{-1} cm^{-2} Å^{-1} arcsec^{-2}, while the interval between contours corresponds to a factor $10^{0.2}$ or 0.5 mags. Labels give observed wavelengths.

UV image of Smith & Cornett (1982). We have selected a small sample of well-known Virgo cluster galaxies from this image and have constructed contour maps for simulations at redshift 0.5, 0.75, and (where possible) 1.2. The galaxies chosen are M100, NGC 4254, NGC 4472, M87, the close pair NGC 4647 + NGC 4649, and the close pair NGC 4569 + IC 3583.

Table 1 lists the galaxies whose UV images are used in the simulations, their Hubble types, the resolution of the UV images, the distance to the galaxy, the observed flux in the near-UV band, and references to published papers.

2.2. *Simulations Derived from Near-UV Images Obtained by UIT Prototypes*

Figures 2–11 show contour maps of the HST and ground-based simulations based on the 2500 Å images of M101, M51, M31, M33, and M83 obtained by the UIT prototype instruments. The monochromatic surface brightness I_λ in ergs s^{-1} cm^{-2} Å^{-1} arcsec^{-2} from the UV imagery is corrected to various redshifts assuming that $I_\lambda \sim (1 + z)^{-5}$ (Peebles 1971). This very strong redshift dependence, which is independent of the choice of H_0 or q_0, can be the source of strong selection effects (Pritchet & Kline, 1981; Wright 1985; Weedman & Williams 1987; Phillipps, Davies & Disney 1990). For all our simulations, we consider only those parts of the galaxy image which lie above a realistic working threshold relative to the sky background. These thresholds are described in more detail below.

A sky background level has been determined for each UV image and subtracted before smoothing. The surface brightness increases by a factor of 1.58 (0.2 dex or 0.5 mag) between successive contour levels. The axis labels on Figures 2–11 are in arcseconds from an origin near the galaxy nucleus. For the HST simulations, the lowest contour plotted is at surface brightness level 3.0×10^{-20} ergs s^{-1} cm^{-2} Å^{-1} arcsec^{-2}, about a factor of 80 below the typical orbital sky background value of 23 mag arcsec^{-2} in the V band quoted by Griffiths (1985). For the ground-based simulations, the lowest contour is at a surface brightness threshold of 5.75×10^{-20} ergs s^{-1} cm^{-2} Å^{-1} arcsec^{-2}, equivalent to 27 mag arcsec^{-2}, or about a factor of 100 below the sky level at high Galactic latitude at a dark site in the V band (O'Connell 1987). The signal-to-noise ratio of the original UV data precludes extending our models to a surface brightness level comparable to the Tyson and Seitzer (1988) deep CCD survey, which has ~ 6 times lower sky threshold.

The angle subtended by an object of fixed linear size is minimized at redshift $z = 1.25$. For higher redshifts the angle subtended increases. Thus, the contour maps derived for the simulations at redshifts 0.5, 0.75, and 1.2 can also be applied to

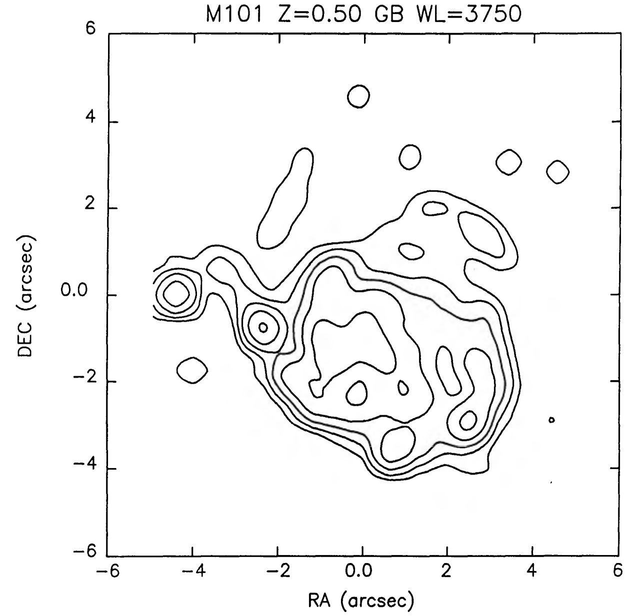

FIG. 3*a*

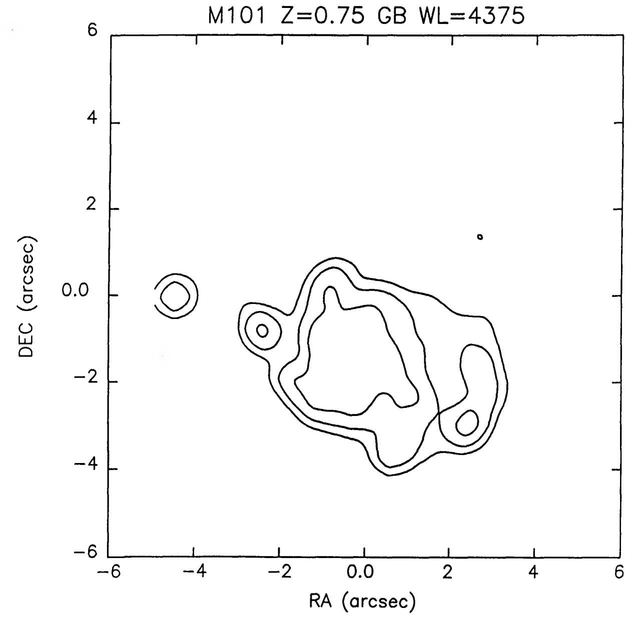

FIG. 3*b*

FIG. 3.—Contour maps at ground-based high resolution of simulations based on UIT-prototype images of M101 for (*a*) $z = 0.5$ and (*b*) $z = 0.75$. In all maps, the lowest contour level surface brightness is 5.75×10^{-20} ergs s^{-1} cm^{-2} Å^{-1} arcsec^{-2}, while the interval between contours corresponds to a factor of $10^{0.2}$. Labels give observed wavelengths.

redshifts 3.2, 2.1, and 1.6, respectively, where the angular scale is the same as the model constructed for the lower redshift. The surface brightness threshold and the total flux decrease as $(1 + z)^{-5}$, while the wavelength of observation increases as $1 + z$. Hence, the $z = 0.75$ simulations can be applied at redshift $z = 2.1$ for the 0.057 times lower thresholds of 1.7×10^{-21} ergs s^{-1} cm^{-2} Å^{-1} arcsec^{-2} for ST simulations or 3.3×10^{-21}

TABLE 2

FLUXES FOR DIFFERENT REDSHIFTS AND THRESHOLDS FROM UIT PROTOTYPE NEAR-UV IMAGES

Galaxy	Observatory	Threshold Surface[a]	$z = 0.5$ Flux[b]	$z = 0.75$ Flux	$z = 1.20$ Flux
M101	ST	3.0	68.0	21.3	4.2
		0.0	74.0	26.4	7.6
		30.0	29.0	2.3	...
M101	GB	5.75	64.1	18.1	0.5
M51	ST	3.0	67.9	24.2	6.0
		0.0	69.8	24.9	7.0
		30.0	56.3	14.5	1.0
M51	GB	5.75	63.1	21.2	4.7
M83	ST	3.0	23.5	8.1	2.1
		0.0	23.7	8.4	2.4
		30.0	20.2	6.0	0.5
M83	GB	5.75	22.9	7.7	1.7
M31	ST	3.0	3.0	0.7	0.06
		0.0	3.2	1.1	0.3
		30.0	0.4	0.06	...
M31	GB	5.75	1.1	0.02	...
M33	ST	3.0	7.9	2.6	0.5
		0.0	8.2	2.7	0.8
		30.0	4.2	0.6	...
M33	GB	5.75	7.0	2.0	...

[a] Threshold surface brightness in units of $\times 10^{-20}$ ergs s^{-1} cm^{-2} Å^{-1} arcsec^{-2}. A zero threshold surface brightness is the limiting case of no uncertainty in the measurement of the sky background.

[b] All tabulated fluxes in units of $\times 10^{-19}$ ergs s^{-1} cm^{-2} Å^{-1}.

for GB. Total fluxes decrease by the same 0.057 factor, while the observed wavelength increases to 7750 Å.

For each simulated galaxy image, the total flux from those pixels above the adopted surface brightness threshold is given in Table 2, along with the total fluxes for a zero threshold and for 10 times the adopted threshold. Note that the total fluxes for the case of zero threshold can be computed from the total observed fluxes given in Table 1, by scaling with $(1 + z)^{-5}\theta_z^2/R^2$, where θ_z is computed from equation (1) and the UV resolution (R) is also in Table 1.

A brief discussion of the results for each of the five galaxies observed by the UIT prototypes follows. In each case, the HST image simulations show greater detail with more contour levels because of the better HST resolution and the lower HST sky background. Labels above each figure give the redshift, the resolution assumed (HST or GB), and the observed wavelength. Where the simulations required degradation of the resolution of the original UV images, we achieved the proper resolution by applying a boxfilter twice. Unresolved sources then have profiles like that of the filter. This is the reason for the "boxy" shape of the contours of unresolved sources in some cases.

2.2.1. *M101*

The Sc I galaxy, M101, is the largest of the five galaxies observed in the UV. A similar system at $z = 0.5$ (Figs. 2*a* and 3*a*) would be $\sim 8''$ in diameter. Almost the entire spiral arm system is above the detection threshold at this redshift. At $z = 0.75$ (Figs. 2*b* and 3*b*) the outer spiral arms fall below the detection limit, but most of the disk plus the brightest OB complexes are detectable. At $z = 1.2$ with HST resolution (Fig. 2*c*), only the inner disk and the brightest H II regions are detectable. At ground-based resolution, the galaxy is not visible, because of the higher sky and lower resolution.

At HST resolution, M101 would probably remain recognizable as an Sc galaxy to $z \sim 1.2$. However, with ground-

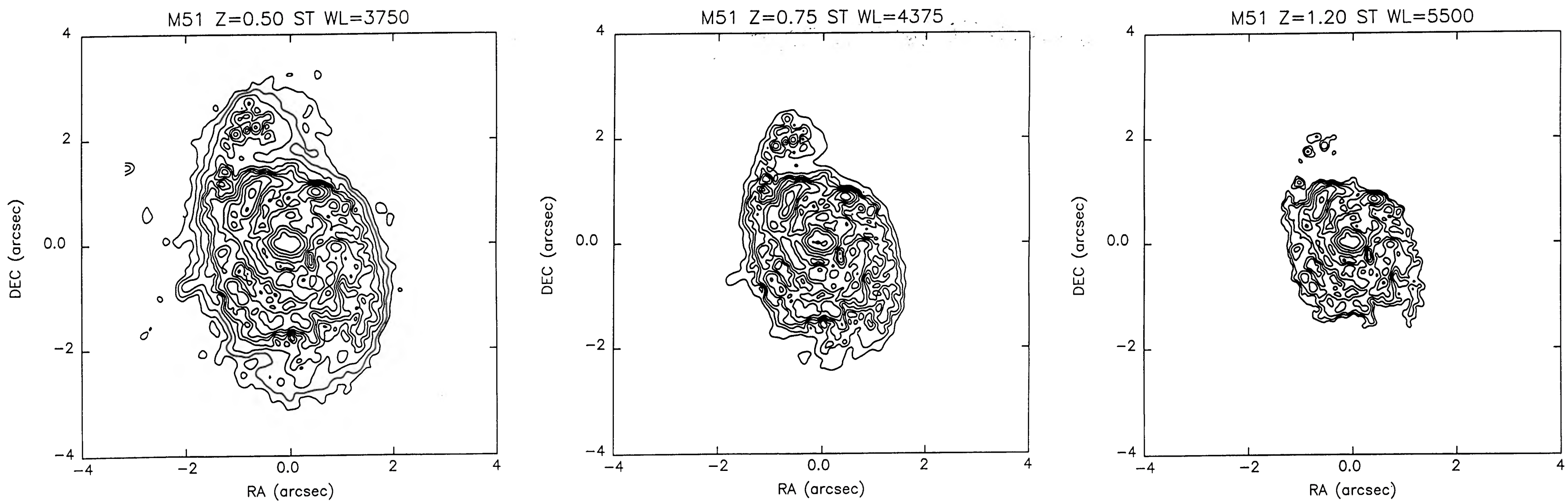

FIG. 4.—Contour maps at HST WFPC resolution of simulations based on UIT-prototype near-UV image of M51, as in Fig. 2

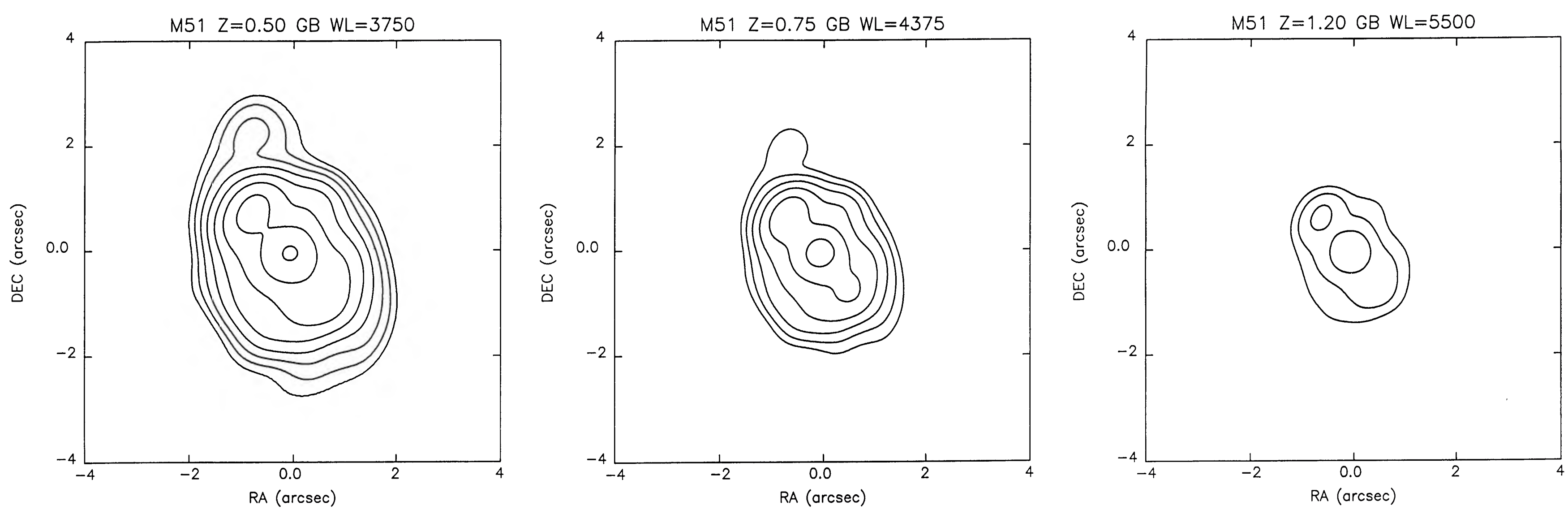

FIG. 5a FIG. 5b FIG. 5c

FIG. 5.—Contour maps at GB resolution of simulations based on UIT-prototype near-UV image of M51, for (*a*) $z = 0.5$, (*b*) $z = 0.75$, and (*c*) $z = 1.20$

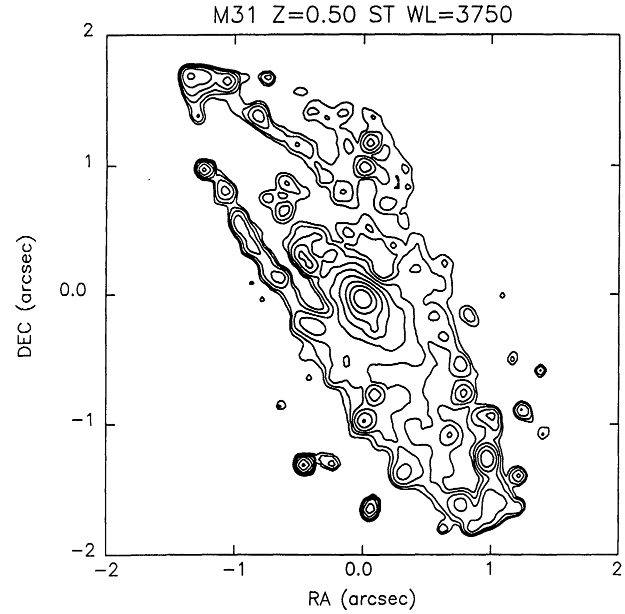

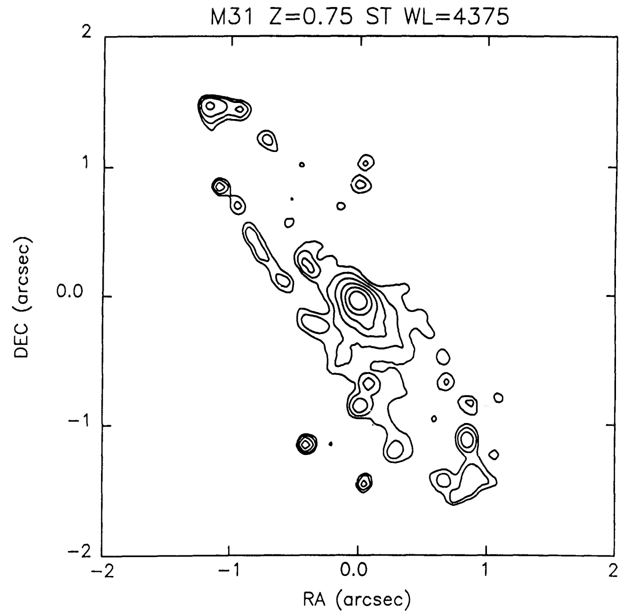

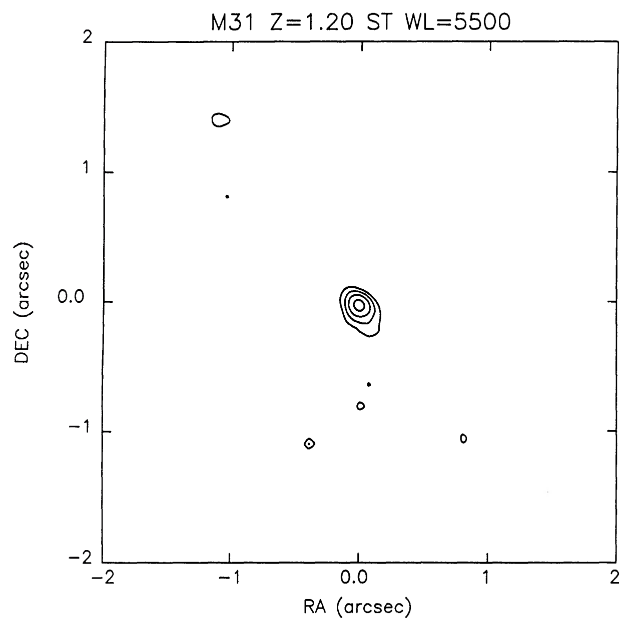

FIG. 6.—Contour maps at HST WFPC resolution of simulations based on UIT-prototype near-UV images of M31, as in Fig. 2.

based resolution, its correct classification would be in doubt at $z > 0.5$. At higher redshifts, only the brightest OB complexes remain visible in the GB images; and the galaxy could be confused with an irregular galaxy (probably one at lower redshift) or an interacting *group* of galaxies.

2.2.2. *M51*

The M51 system subtends an angle of $\sim 5''$ at $z = 0.5$ (Figs. 4*a* and 5*a*). As in the case of M101, almost the entire system is above the detection threshold at this redshift. At redshift $z = 0.75$ (Figs. 4*b* and 5*b*), only the outermost regions of both galaxies fall below the detection threshold. At $z = 1.2$ in the HST simulation (Fig. 4*c*), the disk of M51 and the nuclear region of the companion are visible, while in the GB simulation (Fig. 5*c*) even the nucleus of the companion is undetectable.

In all these simulations, the companion galaxy NGC 5195, which is responsible for perturbing the spiral structure of M51, is rather inconspicuous, as is apparent in the UV/optical comparisons published in Bohlin et al. (1990a). Since the late-type galaxy NGC 5195 has a relatively young stellar population, its faintness in the rest-frame UV is evidently caused by obscuration from dust. In the case of many interacting systems viewed at high redshift, the physical nature of the interaction may not be obvious because of such *k*-correction effects.

2.2.3. *M31*

The HST simulations show M31 (Figs. 6*a*–6*c*) dominated by the nuclear bulge and a surrounding ring of H II regions and OB associations. Because the prominence of the bulge diminishes with respect to the disk owing to the *k*-correction, the

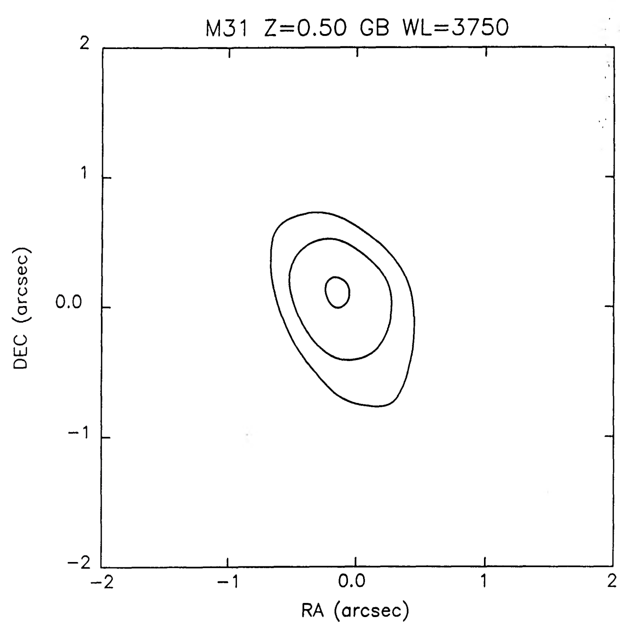

FIG. 7.—Contour map at GB high resolution of simulations based on UIT-prototype near-UV images of M31, for $z = 0.5$ as in Fig. 3.

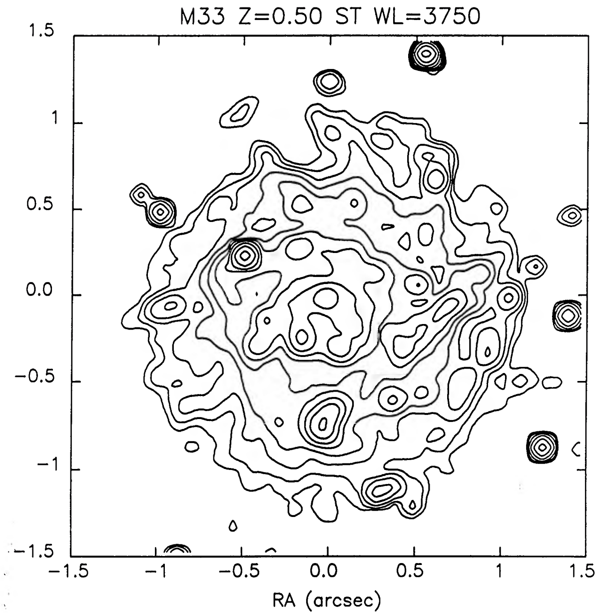

FIG. 8*a*

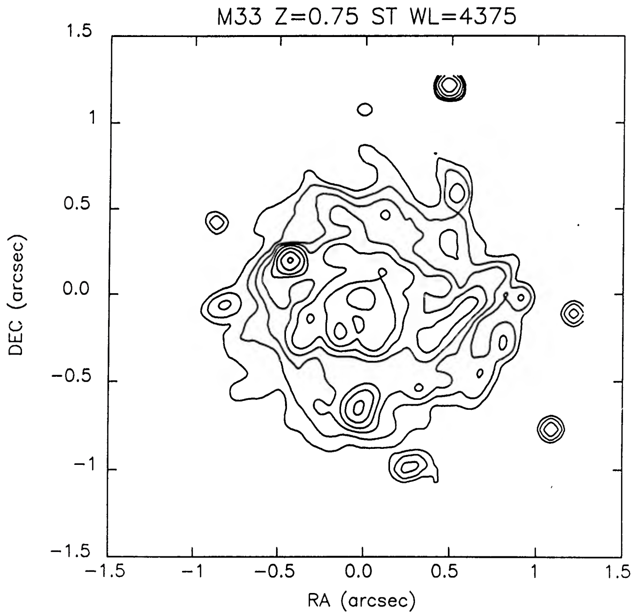

FIG. 8*b*

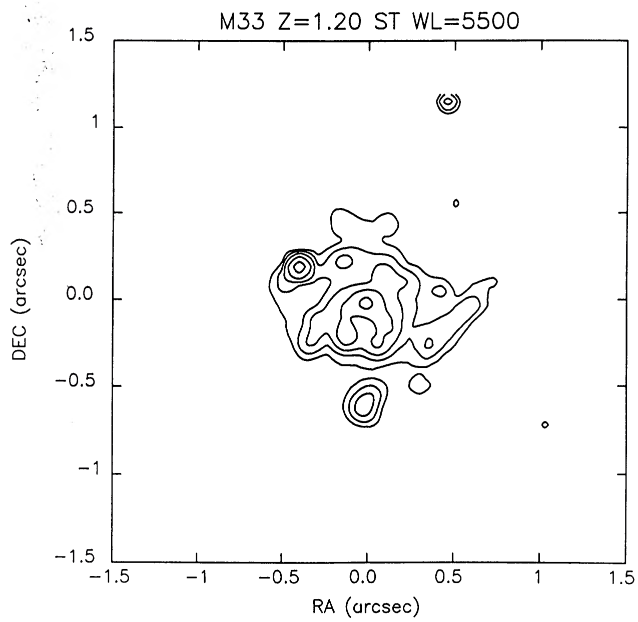

FIG. 8*c*

FIG. 8.—Contour maps at HST WFPC resolution of simulations based on UIT-prototype near-UV image of M33 for redshifts (*a*) $z = 0.5$, (*b*) $z = 0.75$, and (*c*) $z = 1.20$, as in Fig. 2.

Hubble type assigned would be later than its rest frame V band classification of Sb. At $z = 1.2$, only the nuclear bulge and the brightest spiral arm sources are above threshold. As in the case of M101, the galaxy could be mistaken for a group of separate objects. In the GB simulation at $z = 0.5$ (Fig. 7), only the nuclear bulge is above threshold, over an area of dimension $\sim 2''$. The bulge appears similar to an elliptical galaxy but with an asymmetry which still suggests a disklike character. The apparent morphological type of this galaxy would depend strongly on the spatial resolution, as well as the wavelength of observation.

M32, the elliptical companion to M31, is less conspicuous than in the rest frame V band because of its larger k-correction. M32 is visible as a point source in Figure 6*a* at R.A. = 0.0, Decl. = $-1''.0$ but would be hard to distinguish from structure in the disk of M31, except possibly by its color. M32 is not detectable in the ground-based simulation.

2.2.4. *M33*

The M33 contour maps are actually based on a face-on representation (Landsman et al.), constructed using an inclination angle of 55° about an axis at P.A. 23° (Maucherat et al. 1984). Bright foreground stars were identified by comparing the UV images with the optical plates taken for the Space Telescope Guide Star Catalog (Lasker, Jenkner, and Russell 1987) and were removed by replacing circular image areas containing the stars by the local background. In the HST simulation at $z = 0.5$ (Fig. 8*a*), M33 appears as an extended source $\sim 2''$ in diameter with condensations at the nucleus and the brightest OB/H II regions. For higher redshifts (Figs. 8*b*–8*c*), the fraction of this disk above threshold decreases, while the brighter condensations remain visible. The face-on version of M33 should remain recognizable as a spiral at HST resolution to $z \sim 1.5$.

The $z = 0.5$ GB simulation (Fig. 9*a*) shows an extended disk with slight asymmetries in the contours at the positions of the OB associations. At $z = 0.75$ (Fig. 9*b*) only a slightly extended source $\sim 1''.5$ across is visible. M33 could be mistaken for an S0 or even elliptical galaxy at redshifts as low as $z \sim 0.6$.

2.2.5. *M83*

M83 is actively forming stars both in the spiral arms (Bohlin et al. 1990b) and in a nuclear starburst (Bohlin et al. 1983). In the HST simulations at $z = 0.50$, $z = 0.75$, and $z = 1.2$ (Figs. 10*a*–10*c*), the disk appears as an extended source of dimension $\sim 2''$ with peaks discernible at the positions of bright H II regions and OB associations. The central starburst is prominent. In the GB simulations (Figs. 11*a*–11*c*), M83 appears as an extended disk of dimension 1–2″, peaking at the unresolved nuclear starburst with no substructure apparent in the disk.

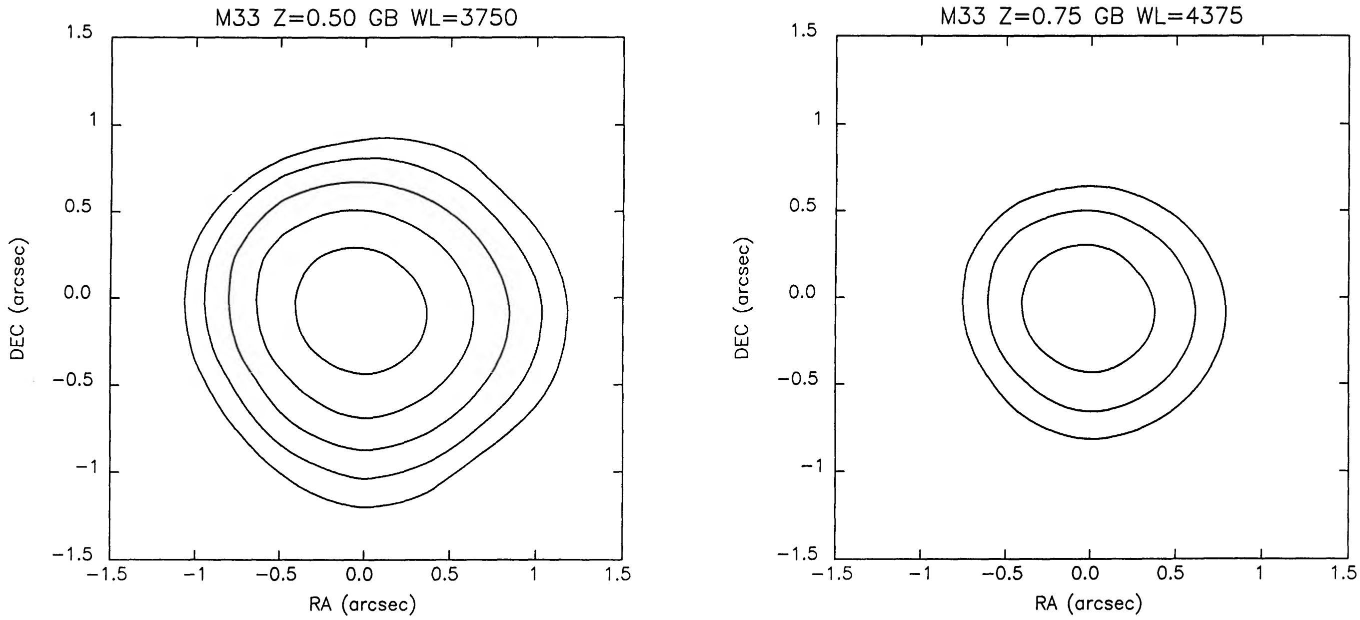

FIG. 9.—Contour maps at GB high resolution of simulations based on UIT-prototype near-UV image of M33 for redshifts (*a*) $z = 0.5$ and (*b*) $z = 0.75$, as in Fig. 3.

In none of the images is the rest-frame *V* band bar prominent. While the galaxy would be recognizable as a late-type spiral, at least at HST resolution up to $z = 1.2$, its barred character might elude detection.

2.3. *Simulations Derived from the Far-UV Images*

The far-UV UIT prototype images ($\lambda \sim 1500$ Å) can be used to simulate optical images of galaxies at redshifts $z = 1.5$, 1.9, and 2.67, where the observed wavelengths are 3750, 4375, and 5500 Å. Figures 12–13 show the simulated high-redshift optical images of M33 and M83. HST and GB simulations are shown for both galaxies at all redshifts for which a significant portion of the galaxy is above the surface brightness threshold. Fluxes above threshold for the far-UV simulations are given in Table 3. No simulations were constructed using the M31 far-UV data, because the disk regions of the images were strongly affected by artifacts caused by the crash landing of the payload. These images (see Bohlin et al. 1985) show a bulge whose profile is indistinguishable from that seen in the near-UV, surrounded by a narrow ring of the brightest OB associations.

TABLE 3

FLUXES FOR DIFFERENT REDSHIFTS AND THRESHOLDS FROM UIT PROTOTYPE FAR-UV IMAGES

Galaxy	Observatory	Threshold Surface[a]	$z = 1.5$ Flux[b]	$z = 1.92$ Flux	$z = 2.67$ Flux
M83.........	ST	3.0	1.74	0.70	0.12
		0.0	1.87	0.90	0.35
		30.0	0.40	0.09	...
M83.........	GB	5.75	1.19	0.18	...
M33.........	ST	3.0	0.61	0.15	...
		0.0	0.9	0.45	0.17
		30.0	...	...	...
M33.........	GB	5.75	0.28	...	...

[a] Threshold surface brightness in units of $\times 10^{-20}$ ergs s^{-1} cm^{-2} Å^{-1} arcsec^{-2}. A zero threshold surface brightness is the limiting case of no uncertainty in the measurement of the sky background.

[b] All tabulated fluxes in units of $\times 10^{-19}$ ergs s^{-1} cm^{-2} Å^{-1}.

2.3.1. *M33*

When observed at $z = 1.5$ at 3750 Å by HST (Fig. 12*a*), M33 would show an inner disk of diameter $\sim 1''.5$, peaking at the brightest H II regions. When observed at $z = 1.92$, wavelength 4375 Å (Fig. 12*b*), only the central $0''.5$ of the disk is visible, while the brightest H II regions are seen as separate sources. As observed from the ground at $z = 1.5$, M33 would be a faint unresolved source barely above threshold at wavelength 3750 Å and is not detectable above the threshold at higher *z*.

2.3.2. *M83*

When observed by HST at redshift $z = 1.50$ (Fig. 14*a*), M83 has a diameter of $\sim 1''$; but the spiral arms and the major H II regions within them, as well as the nuclear starburst are clearly visible. As the redshift increases to 1.92 and 2.67 (Figs. 14*b*–14*c*), lower surface brightness outer regions and interarm regions fall below the threshold of detectability. Even at $z = 2.67$ (Fig. 14*c*), M83 would be classified as a spiral galaxy. The simulated M83 GB images for redshifts $z = 1.5$–2.67 (Figs. 14*a*–15*c*) show the nuclear starburst plus the galactic disk as a single partially resolved source.

2.4. *Simulations Derived from Wide Field Virgo Cluster Image*

Figures 16–21 show surface brightness contour maps of the selected Virgo cluster galaxies for simulations of ground-based "low-resolution" ($1''.9$ FWHM) imaging at redshifts 0.50, 0.75, and 1.20. The fluxes above the surface brightness threshold have been determined for each simulation and are given in Table 4. A brief description of the results for the individual galaxies follows.

2.4.1. *M100*

The simulation based on the M100 UV data subtends $\sim 6''$–$7''$ for $z = 0.5$–0.75 (Fig. 16*a*–16*b*). At the simulated resolution of $1''.9$, substructure in the spiral arms is not resolved. At $z = 1.2$ (Fig. 16*c*), the galaxy size shrinks to $\sim 4''$.

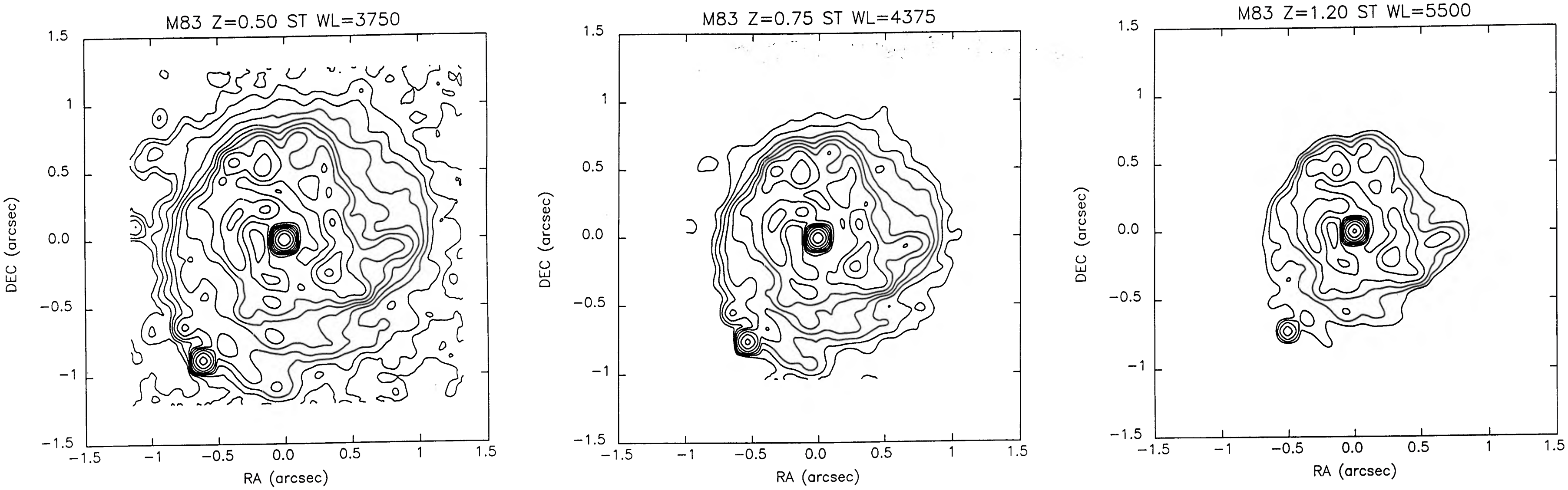

FIG. 10.—Contour maps at HST WFPC resolution of simulations based on UIT-prototype near-UV image of M83, as in Fig. 2

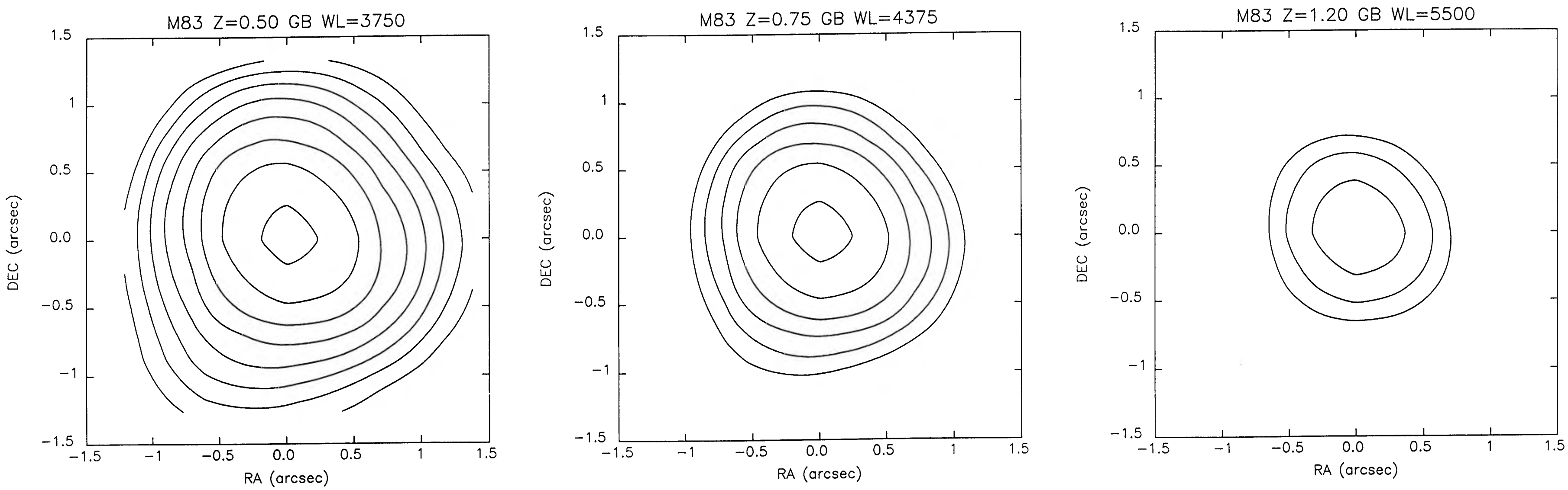

FIG. 11.—Contour maps at GB high resolution of simulations based on UIT-prototype near-UV image of M83, as in Fig. 3

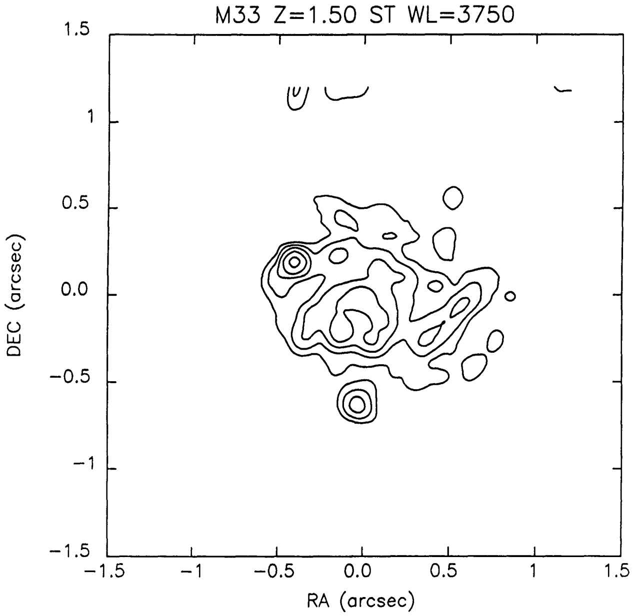

FIG. 12*a*

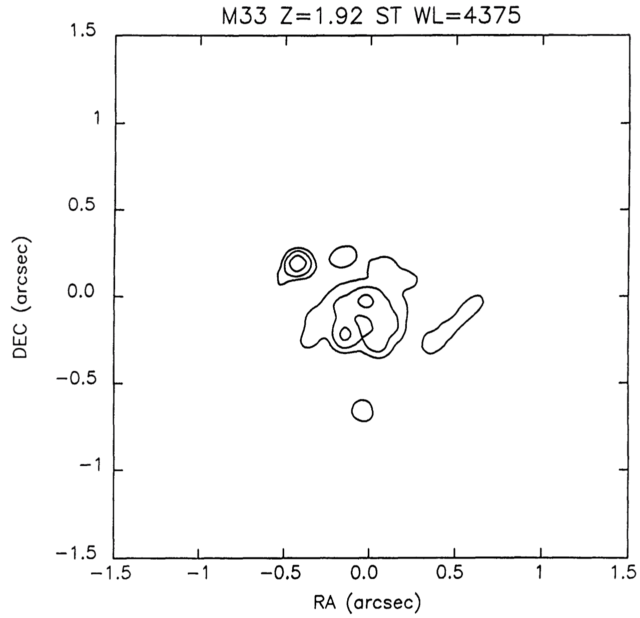

FIG. 12*b*

FIG. 12.—Contour maps, as in Fig. 2, at HST WFPC resolution of simulations based on UIT-prototype far-UV image of M33 for (*a*) $z = 1.5$ and (*b*) $z = 1.92$

2.4.2. *NGC 4254*

The bright spiral galaxy NGC 4254 also subtends an angle of $\sim 6''$ at $z = 0.5$–0.75 (Figs. 17*a*–17*b*). At $z = 1.2$ (Fig. 17*c*), the disk is detectable over $\sim 3''$. Again, no substructure is apparent at the simulated resolution of 1".9.

2.4.3. *NGC 4472*

NGC 4472 is a giant elliptical galaxy with an ultraviolet turnup (Oke, Bertola, and Capaccioli 1981). At $z = 0.5$ (Fig. 16*a*), it is detectable over an angle of $\sim 3''$. NGC 4472 is detectable at $z = 0.75$ (Fig. 18*b*), but not above threshold at $z = 1.2$.

2.4.4. *M87*

M87 is a giant elliptical galaxy with a nonthermal nuclear jet and a UV turnup. The high-redshift simulations based on the M87 data (Fig. 19*a*–19*b*) are similar to those base on the NGC 4472 data).

Figures 16–19 show that there is very little morphological distinction between Sc galaxies and giant ellipticals at the simulated resolutions. Identifications could, in principle, be made by spectra or colors. However, the extremely low surface brightness of even luminous galaxies like M87 might be too faint for useful spectroscopy.

2.4.5. *NGC 4647 and NGC 4649*

NGC 4647, the northern galaxy, is a face-on spiral, while NGC 4649 is a bright elliptical. Their apparent separation at high redshift is $\sim 3''$. Although NGC 4649 is brighter by ~ 2 mag in the rest-frame *B* band (de Vaucouleurs, de Vaucouleurs, and Corwin 1976), the two galaxies are equally bright above threshold in the $z = 0.5$ (Fig. 20*a*) simulation, and NGC 4647 is brighter by almost a factor of 2 at $z = 0.75$ (Fig. 18*b*). Neither galaxy is above threshold at $z = 1.2$.

TABLE 4

FLUXES ABOVE THRESHOLD DERIVED FROM VIRGO CLUSTER NEAR-UV IMAGES

Galaxy	$z = 0.5$ Flux[a]	$z = 0.75$ Flux	$z = 1.20$ Flux
M87	6.8	1.9	...
M100	72.0	27.0	3.1
N4472	6.8	0.7	...
N4649	8.7	1.3	...
N4647	9.7	2.4	...
N4254	66.0	27.0	5.0
N4406	0.5	...	...
N4569	11.0	2.1	...
IC 3583	8.5	3.1	...

[a] All tabulated fluxes in units of $\times 10^{-19}$ ergs s^{-1} cm^{-2} Å^{-1}.

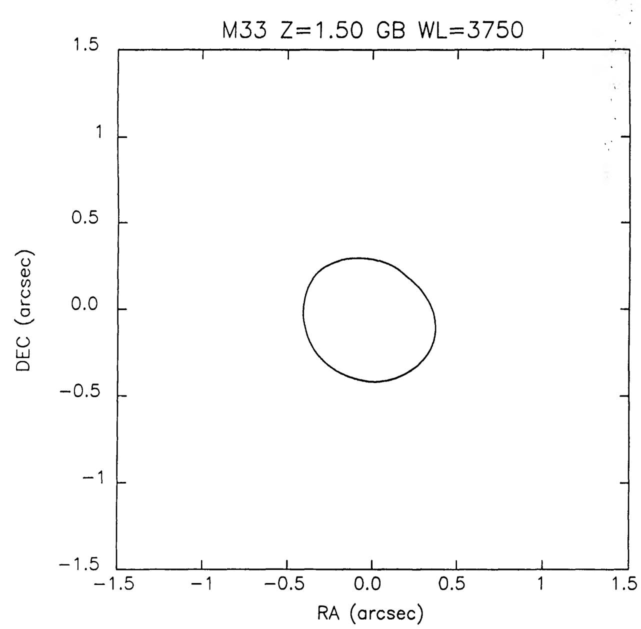

FIG. 13.—Contour map, as in Fig. 3, at GB high resolution of simulation based on UIT-prototype far-UV image of M33 for $z = 1.5$.

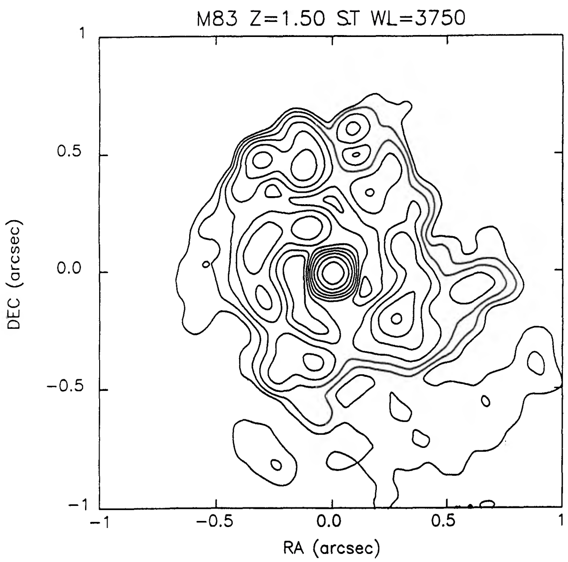

FIG. 14*a*

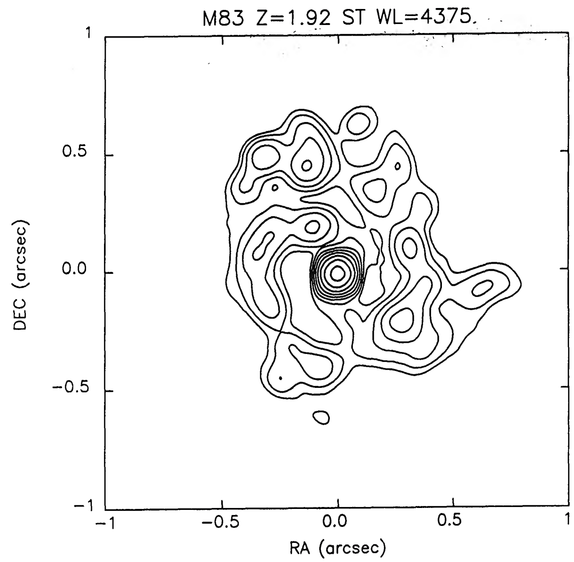

FIG. 14*b*

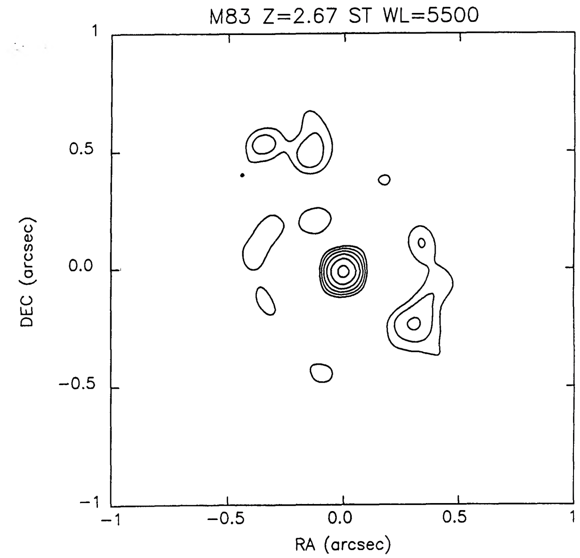

FIG. 14*c*

FIG. 14.—Contour maps, as in Fig. 2, at HST WFPC resolution of simulations based on UIT-prototype far-UV image of M83 for (*a*) $z = 1.5$, (*b*) $z = 1.92$ and (*c*) $z = 2.67$

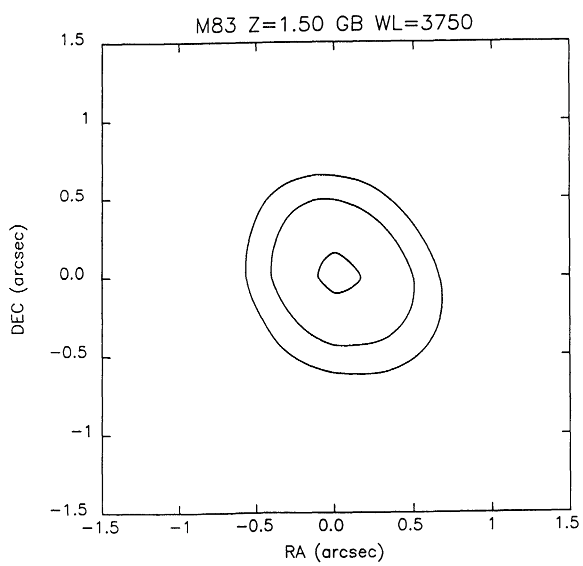

FIG. 15*a*

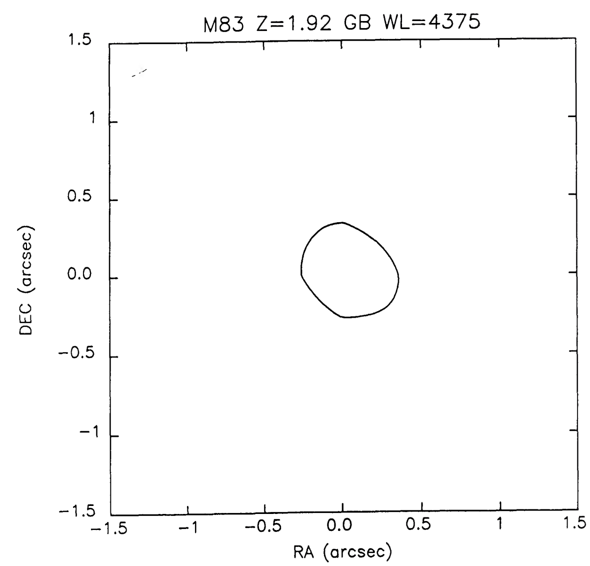

FIG. 15*b*

FIG. 15.—Contour maps, as in Fig. 3, at GB high-resolution of simulations based on UIT-prototype far-UV image of M83 for (*a*) $z = 1.5$ and (*b*) $z = 1.92$

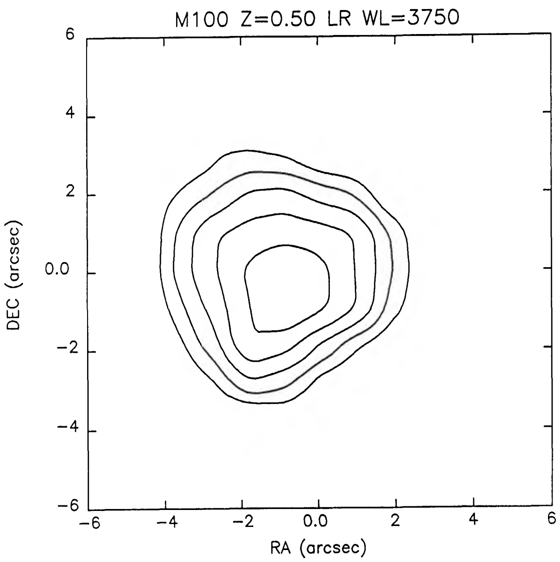

FIG. 16*a*

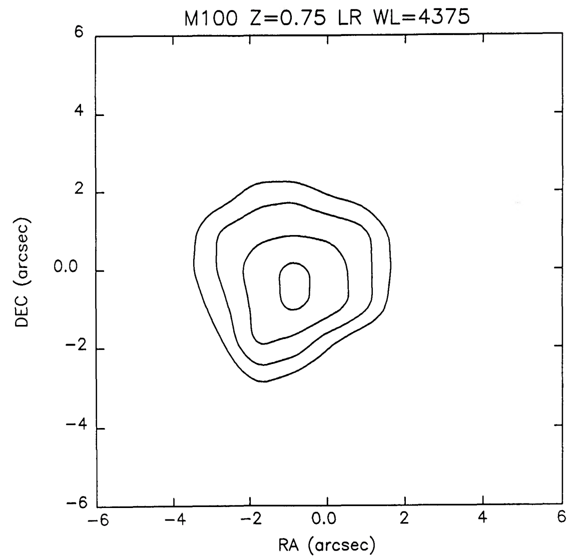

FIG. 16*b*

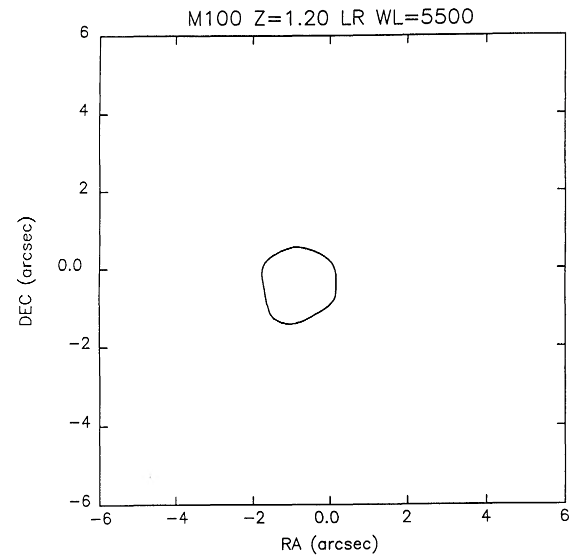

FIG. 16*c*

FIG. 16.—Contour maps with 1"9 resolution (LR) of simulations based on the Virgo cluster near-UV image of the field near M100 for (*a*) $z = 0.5$, (*b*) $z = 0.75$, and (*c*) $z = 1.2$

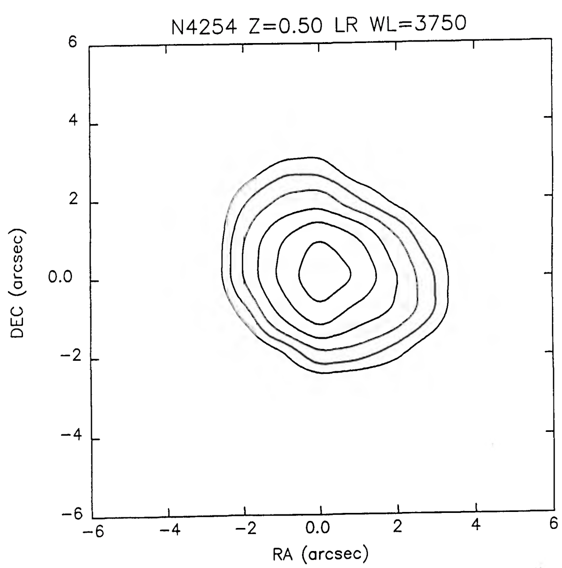

FIG. 17*a*

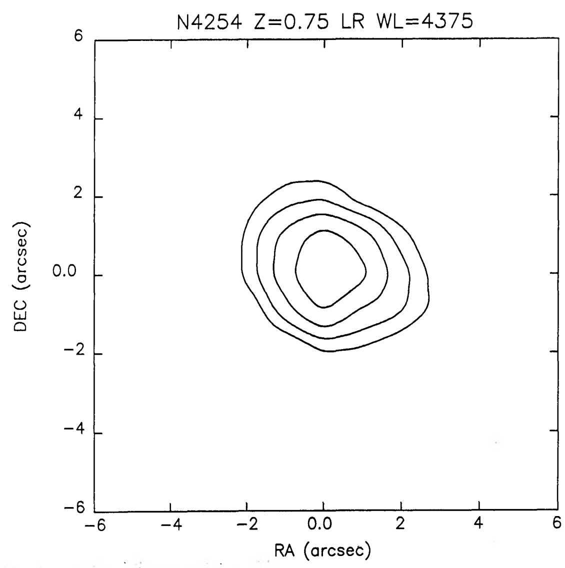

FIG. 17*b*

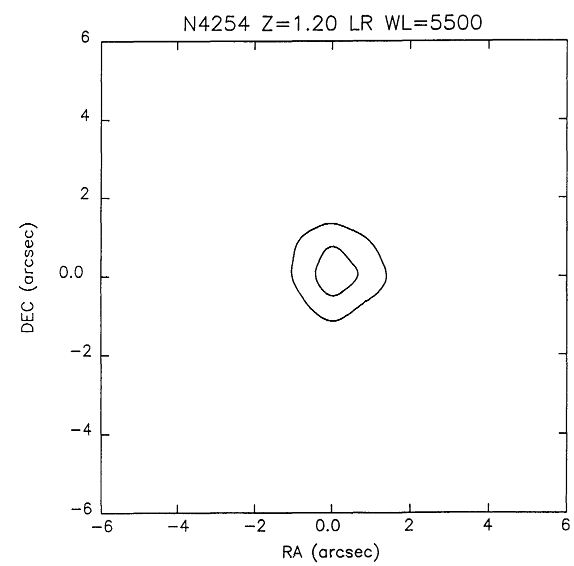

FIG. 17*c*

FIG. 17.—(*a*–*c*) Contour maps with 1"9 resolution of simulations based on the Virgo cluster near-UV image of the field near NGC 4254, as in Fig. 16

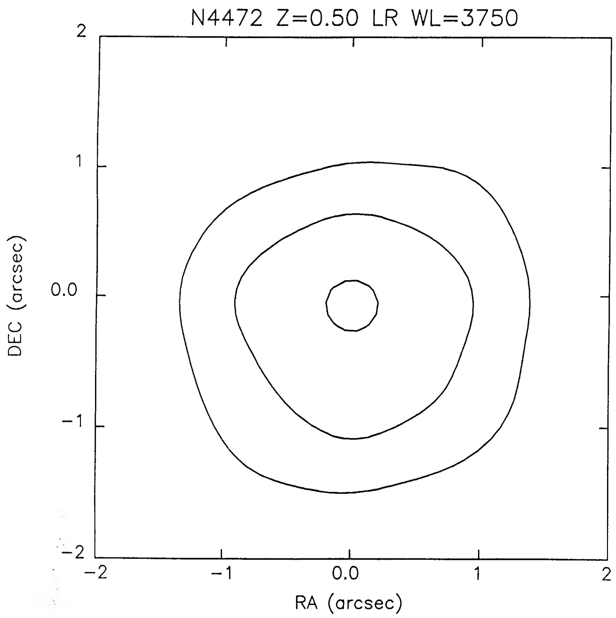

FIG. 18a

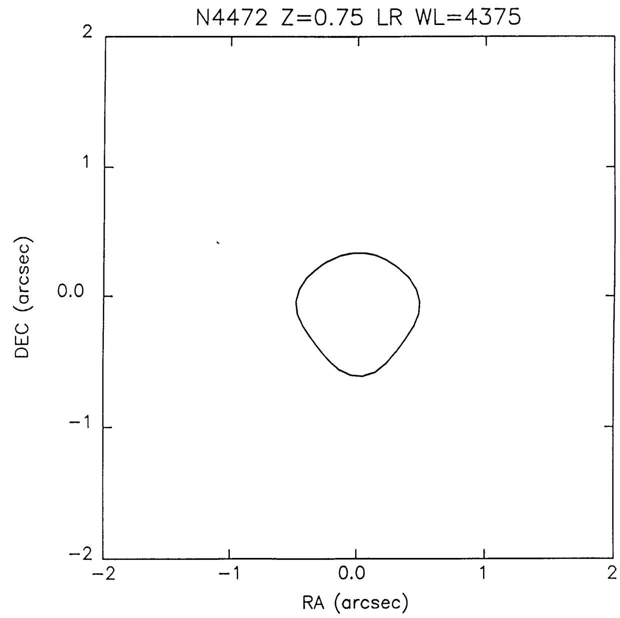

FIG. 18b

FIG. 18.—Contour maps with 1".9 resolution of simulations based on the Virgo cluster near-UV image of the field near NGC 4472, for (*a*) $z = 0.5$ and (*b*) $z = 0.75$, as in Fig. 16.

2.4.6. *NGC 4569 and IC 3583*

NGC 4569 is an Sab galaxy, while IC 3583 (the northernmost object) is a Magellanic irregular. The galaxies are separated by $\sim 6''$ and each subtends an angle of $\sim 3''$ at high redshift. The flux measurements above threshold in Table 3 indicate that, while the NGC 4569 analog is brighter by a factor of 1.3 at $z = 0.5$ (Fig. 21*a*), the IC 3583 analog is brighter by a factor of 1.5 at $z = 0.75$ (Fig. 21*b*). Neither galaxy is above threshold at $z = 1.2$.

3. DISCUSSION

Our simulations show that the morphology of objects observed at high redshift is strongly influenced by two effects, apart from the role played by evolution of their stellar populations. These effects are the *k*-correction (that is, the dependence of morphology on rest wavelength) and the strong dependence of surface brightness on redshift. The faintness of the predicted surface brightness means that the night sky threshold has a dominant influence on the results. While the

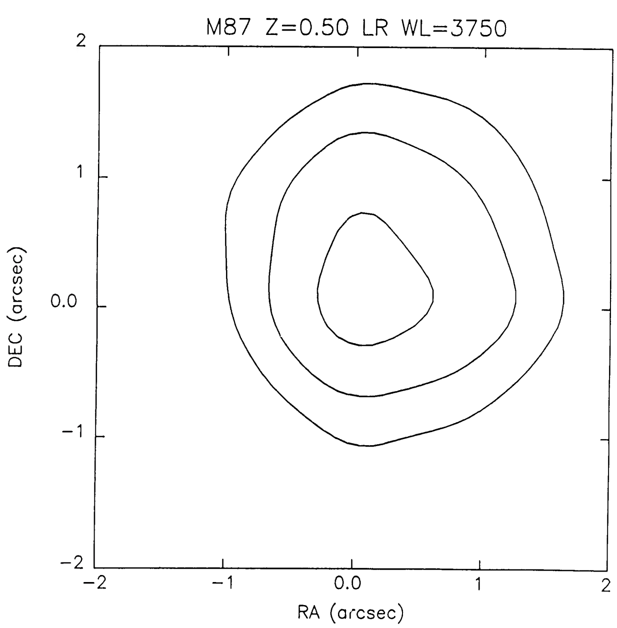

FIG. 19a

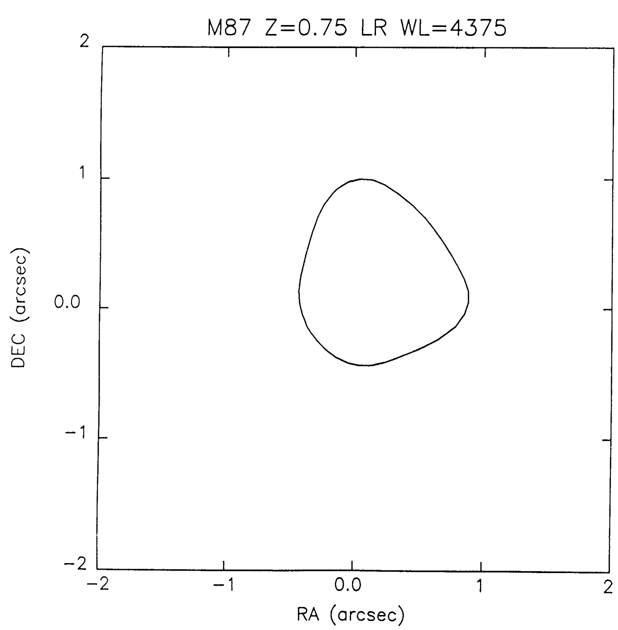

FIG. 19b

FIG. 19.—Contour maps with 1".9 resolution of simulations based on the Virgo cluster near-UV image of the field near M87, for (*a*) $z = 0.50$ and (*b*) $z = 0.75$, as in Fig. 16.

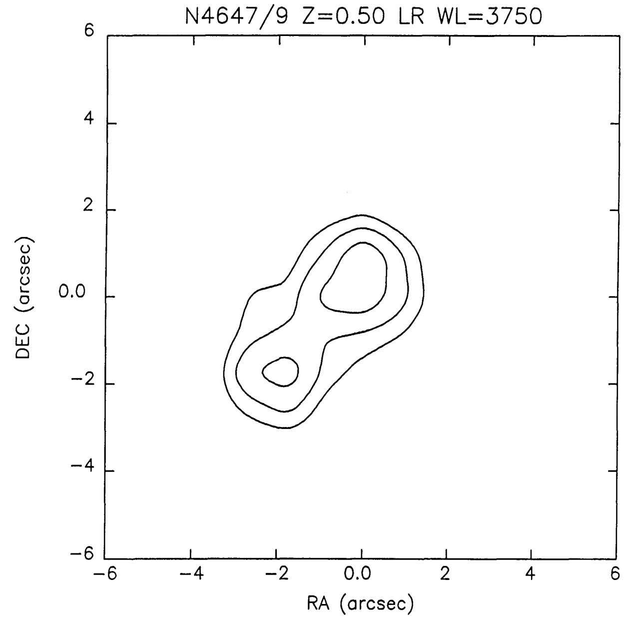

FIG. 20*a*

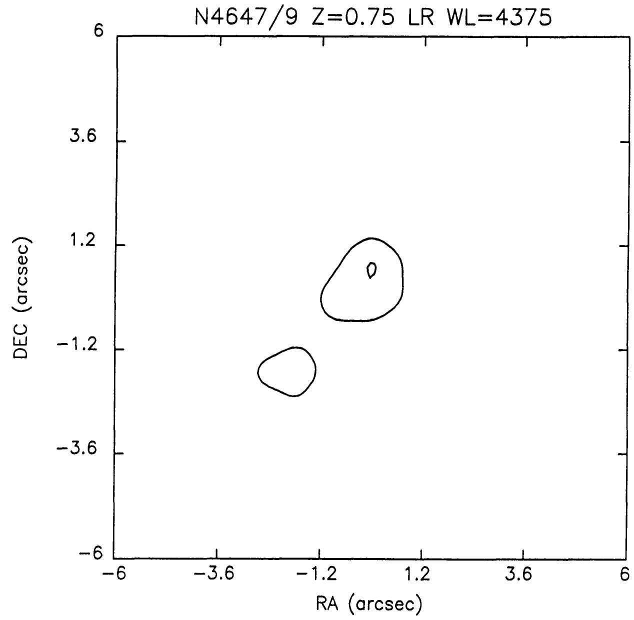

FIG. 20*b*

FIG. 20.—Contour maps with 1″.9 resolution of simulations based on the Virgo cluster near-UV image of the field near NGC 4647 and NGC 4749, for (*a*) $z = 0.5$ and (*b*) $z = 0.75$, as in Fig. 16.

effects of the *k*-correction could be minimized by observing at longer (near-infrared) wavelengths with a ground-based telescope, the bright telluric OH emission raises the sky background. However, at 9000 Å WFPC images will not have the OH enhancement of the sky background.

The assessment of the physical situation in high-redshift systems will be problematic. Spiral galaxies can be mistaken for S0 or E types or, even for irregulars; early-type spirals can be mistaken for later types; barred galaxies can be mistaken for normal; interacting systems can be mistaken for isolated ones; and single systems can be mistaken for multiple ones. The amplitudes of these "morphological transformations" are perhaps surprisingly large.

Apart from questions of morphology, the detectability of distant objects with local analogs is summarized in Tables 2–4. Since the smaller galaxy M83 is detectable by HST at $z = 2.67$ and by ground-based instruments at $z = 1.92$, M101 and M51 analogs should also be detectable at these large redshifts. The

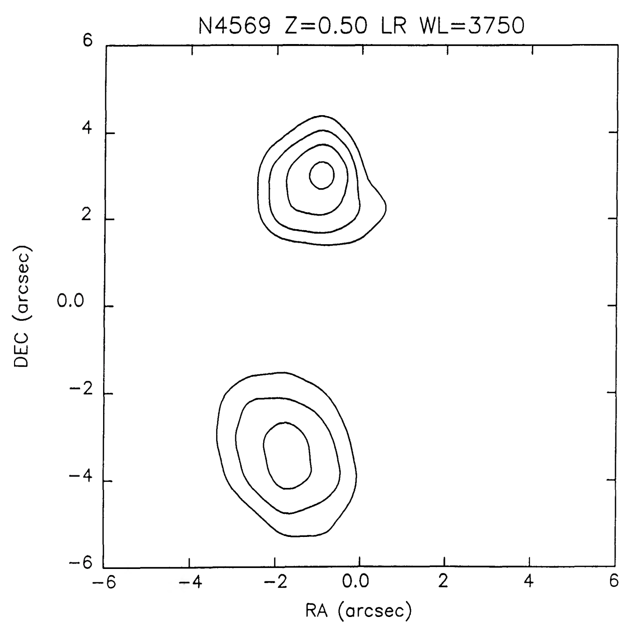

FIG. 21*a*

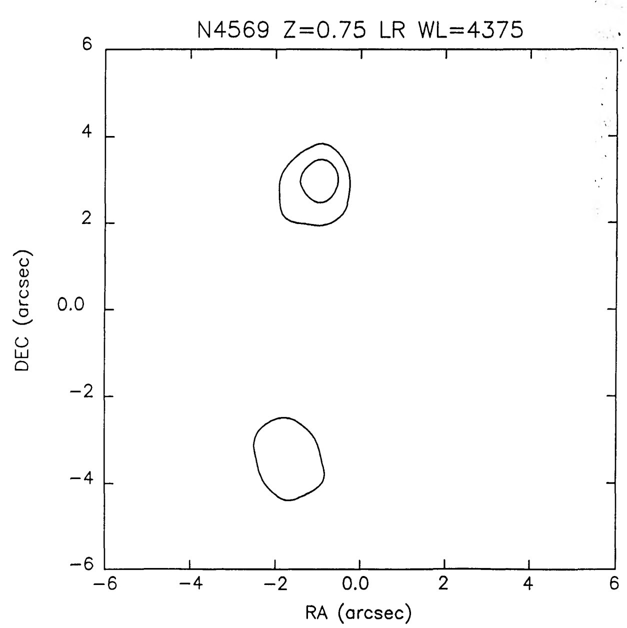

FIG. 21*b*

FIG. 21.—Contour maps with 1″.9 resolution of simulations based on the Virgo cluster near-UV image of the field near NGC 4569 and IC 3583 for (*a*) $z = 0.5$ and (*b*) $z = 0.75$, as in Fig. 16.

simulations derived from the Virgo cluster data and from the spiral galaxies that are similar to M101 illustrate a point made previously by Coleman, Wu, and Weedman (1980) and others: the brightest galaxies in the optical bands at $z \sim 1$ are expected to be spirals, rather than ellipticals. Table 4 shows that the brightest Virgo galaxies in the three simulated optical bandpasses are the spirals M100 and NGC 4254, which are the only galaxies detectable at $z = 1.2$. However, in the restframe *B* band, the brightest three Virgo galaxies are the ellipticals M87, NGC 4472, and NGC 4649.

Additional vacuum-UV imaging of nearby galaxies will be of great value in providing the basic information needed to decipher observations of high-redshift systems.

The funding for the research was provided through NASA RTOP 680-879-11-41, NASA Spacelab Project 680-440-51-02, and NASA grant NAG-5-700 (R. W. O.).

REFERENCES

Bohlin, R. C., Cornett, R. H., Hill, J. K., Hill, R. S., O'Connell, R. W., & Stecher, T. P. 1985, ApJ, 298, L37
Bohlin, R. C., Cornett, R. H., Hill, J. K., O'Connell, R. W., & Stecher, T. P. 1990a, ApJ, 352, 55
Bohlin, R. C., Cornett, R. H., Hill, J. K., Smith, A. M., & Stecher, T. P. 1983, ApJ, 274, L53
Bohlin, R. C., Cornett, R. H., Hill, J. K., & Stecher, T. P. 1990b, ApJ, 381, 154
Bohlin, R. C., Hill, J. K., Stecher, T. P., & Witt, A. N. 1982, ApJ, 255, 87
Bruzual, A., G. 1988, in Towards Understanding Galaxies at High Redshift, ed. R. G. Kron & A. Renzini (Dordrecht: Kluwer Academic), p. 161
Bruzual A. G., & Kron, R. G. 1980, ApJ, 241, 25
Coleman, G. D., Wu, C.-C., & Weedman, D. W. 1980, ApJS, 43, 393
de Vaucouleurs, G., de Vaucouleurs, A., & Corwin, H. G. 1976, Second Reference Catalog of Bright Galaxies (Austin: University of Texas Press)
Griffiths, R. 1985, Wide Field and Planetary Camera Instrument Handbook (Baltimore: Space Telescope Science Institute)
Guth, A. H. 1981, PRev, D23, 347
Hill, J. K., Bohlin, R. C., & Stecher, T. P. 1984, ApJ, 277, 542
Hill, R. S. 1987, Ultraviolet Imaging Telescope Batch Data Reduction: Design and Maintenance (Lanham, MD: ST Systems Corporation; STX-T-25-3002-008-87)
King, C. R., and Ellis, R. S. 1985, ApJ, 288, 456
Landsman, W. B., Bohlin, R. C., Cornett, R. H., Hill, J. K., and Stecher, T. P. 1990, in preparation
Lasker, B. M., Jenkner, H., and Russell, J. L. 1987, Space Telescope Science Institute Preprint Series, 187
Le Fèvre, O., & Hammer, F. 1990, ApJ, 333, L37
Maucherat, A. J., Dubout-Crillon, R., Monnet, G., & Figon, P. 1984, A&A, 133, 341
Neff, S. G., & Hutchings, J. B. 1990, AJ, 99, 1715
O'Connell, R. W. 1987, AJ, 94, 876
Oke, J. B., Bertola, F., & Capaciolli, M. 1981, ApJ, 243, 453
Peebles, P. J. E. 1971, Physical Cosmology (Princeton: Princeton University Press)
Phillipps, S., Davies, J. I., & Disney, M. J. 1990, MNRAS, 242, 235
Pritchet, C., & Kline, M. J. 1981, AJ, 241, 25
Rowan-Robinson, M. 1985, The Cosmological Distance Ladder (New York: W. H. Freeman)
Smith, A. M., & Cornett, R. H. 1982, ApJ, 261, 1
Stecher, T. P., Bohlin, R. C., Butcher, H. R., O'Connell, R. W., Roberts, M. S., Smith, A. M., & Parise, R. A. 1983, BAAS, 14, 882
Talbot, R. J., Jenson, E. B., & Dufour, R. J. 1979, ApJ, 229, 91
Thompson, L. A. 1988, ApJ, 324, 112
Tyson, J. A., & Seitzer, P. 1988, ApJ, 335, 552
Weedman, D. W., & Williams, K. L. 1987, ApJ, 318, 585
Wright, E. L. 1985, PASP, 97, 451